Remote Sensing of Environment 287 (2023) 113474

Contents lists available at ScienceDirect

Remote Sensing of Environment

journal homepage: www.elsevier.com/locate/rse

P-band SAR for ground deformation surveying: Advantages and challenges

Yuankun Xu [a,b,*], Zhong Lu [c], Roland Bürgmann [a,b], Scott Hensley [d], Eric Fielding [d], Jinwoo Kim [c]

[a] Department of Earth and Planetary Science, University of California, Berkeley, Berkeley, CA 94720, USA
[b] Berkeley Seismological Laboratory, University of California, Berkeley, Berkeley, CA 94720, USA
[c] Department of Earth Sciences, Southern Methodist University, Dallas, TX 75205, USA
[d] Jet Propulsion Laboratory, California Institute of Technology, Pasadena, CA 91109, USA

ARTICLE INFO

Edited by Jing M. Chen

Keywords:
P-band SAR
InSAR
Forested terrain
Ground deformation
High-gradient deformation
Landslides
Radar penetration depth
Snow

ABSTRACT

Global success of utilizing X/C/L-band InSAR (Interferometric Synthetic Aperture Radar) to survey ground deformation over non-forested terrain in the past two decades, has raised interest in monitoring forested lands, where relatively short-wavelength X/C/L SAR acquisitions often experience strong decorrelation and downgraded InSAR quality. To address this challenge, we considered the long-wavelength P-band SAR and conducted a large-area experiment over diverse terrains of the U.S. West Coast to comprehensively assess P-band SAR's capability for ground deformation surveying. Our results show that P-band InSAR observations greatly outperformed L-band data for identifying ground deformation within forested regions and for measuring spatially high-gradient displacements, such as for slow-moving landslides. Over the entire study area, P-band InSAR helped to discover >200 new landslides that were missing from existing landslide inventories. It also demonstrated high capability of penetrating through shallow snowpack to collect SAR signals from the ground surface beneath. However, P-band data manifested lower sensitivity to subtle deformation, as expected theoretically, and encountered coherence loss resulting from heavy snowpack. Overall, P-band SAR demonstrated to be a highly effective tool for discovering deformation beneath dense forest canopies and for quantifying spatially high-gradient displacements. These findings provide an experimental basis for planning future satellite and airborne P-band SAR missions to enhance the capability to monitor changes of the Earth's surface.

1. Introduction

Rapid technical advancement and global applications of the InSAR (Interferometric Synthetic Aperture Radar) technique in the past two decades has greatly explored and substantiated SAR's value and potential for monitoring earth's surface deformation, ranging from fault slip (e.g., Wright et al., 2004), volcanic unrest (e.g., Lu and Dzurisin, 2014), landslides (e.g., Schlögel et al., 2015), glaciers (e.g., Gray, 2011), aquifer variations (e.g., Amelung et al., 1999), to infrastructure instability (e.g., Perissin et al., 2012). Presently, X, C, and L-band SAR acquisitions dominate the global datasets. However, despite their widespread applications to measuring deformation over non-forested terrains, the X/C/L-band SAR sensors' relatively short wavelengths (3.1–24.2 cm) generally limit their capability to penetrate through dense vegetation to collect relatively stable signals from ground surface, thereby rendering them less effective for surveying densely forested terrains (Xu et al., 2021a; El Hajj et al., 2018; Smith and Jol, 1995). By contrast, P-band SARs with a longer wavelength of 67–139 cm, holds the potential to address this challenge.

In a scheme to comprehensively evaluate P-band SAR's performance for surveying deformation over vegetated terrains, we utilized the NASA/JPL (Jet Propulsion Laboratory)'s UAVSAR (Uninhabited Aerial Vehicle Synthetic Aperture Radar) P-band radar that was formerly called AIRMOSS (Airborne Microwave Observatory of Subcanopy and Subsurface) radar system (Chapin et al., 2012). We utilized the UAVSAR P-band instrument (wavelength of 69.72 cm) to acquire repeat-pass P-band SAR data in multiple regions on the U.S. West Coast (i.e., Washington, Oregon, and California state) and investigated the advantages and challenges of using P-band SAR to detect and quantify ground displacements. The NASA UAVSAR system has two different radar instruments (P-band and L-band) that can be attached to the same piloted Gulfstream airplanes, but only one instrument (either P-band or L-band) can be attached each time. The pod mounted beneath the aircraft houses all the radar electronics, and INU (inertial navigation unit) and GPS receiver in addition to the SAR antenna. Both the L-band and P-band antennas are similar in size and presently only one at a time can fit

* Corresponding author at: Department of Earth and Planetary Science, University of California, Berkeley, Berkeley, CA 94720, USA.
E-mail address: yuankunx@berkeley.edu (Y. Xu).

https://doi.org/10.1016/j.rse.2023.113474
Received 1 June 2022; Received in revised form 10 January 2023; Accepted 17 January 2023
Available online 26 January 2023
0034-4257/© 2023 Elsevier Inc. All rights reserved.

within the pod.

Through comparisons of airborne P-band and L-band SAR results in northern California, and an overall evaluation of P-band InSAR's performance over the U.S. West Coast, our experiments consider direct observations to showcase the unique values of P-band SAR and explain its limitations. The insights gained from our results can also be used to help design future airborne and satellite P-band SAR missions to enhance deformation monitoring capabilities over forested lands globally. The remainder of the paper is organized as follows: Section 2 provides an overview of the study area and the utilized data, Section 3 describes the methods used for the data processing and results evaluation, Sections 4–6 show the results of using the P-band UAVSAR for surveying deformation over vegetated and snow-covered terrains, as well as a comparison with the L-band UAVSAR observations. The discussion and conclusions are presented in Sections 7 and 8, respectively.

2. Study area and data

Multiple dispersed areas across the western part of the U.S. West Coast (i.e., Washington, Oregon, and California) were selected as target regions for this study (Fig. 1). These target areas are dominantly forested by Douglas-fir, with some hemlock/Sitka spruce, alder/maple, and other hardwoods. Most of these tree species are coniferous, evergreen, and can reach 100 m in height and 5 m in diameter (USFS (U.S. Forest Service), 2022). As shown in the 500 m resolution NDVI (Normalized Differential Vegetation Index) map (Fig. 1a; Didan, 2021), which was produced from optical images acquired during 2020 and 2021 summers (June to September), the imaged target areas are dominantly composed of moderately to densely forested terrains with NDVI >0.3 (Fig. 1a). Only a very small fraction of the target areas contain relatively barren terrain and developed land. Elevations of the target areas range from 0 to 2500 m above sea level (Fig. 1b).

We acquired repeat-pass P-band SAR data covering these distributed target areas around 13 November 2020 and 02 May 2021 (± 3 days), respectively, using NASA JPL's left-looking UAVSAR P-band radar system (Table 1). For each round of the acquisitions, we collected 22 segments of P-band SAR data along the designed flight path, with each segment being 14 km wide and 74–123 km long (Fig. 1a). The flight directions are marked on the near-range side of the rectangular flight segments in Fig. 1b. Depending on the specific location, the target areas were covered by one to four flight segments with distinct flight headings and looking angles.

Over the Eel River region (Fig. 1a), in addition to the P-band SAR data, we acquired UAVSAR L-band data with the identical flight settings (i.e., flight direction and look angle) on 27 October 2020 and 13 May 2021, respectively, in order to compare the P-band and L-band SAR results (Table 1). Detailed flight plans and the data acquisitions are accessible from the UAVSAR data portal (JPL (Jet Propulsion Laboratory), 2022).

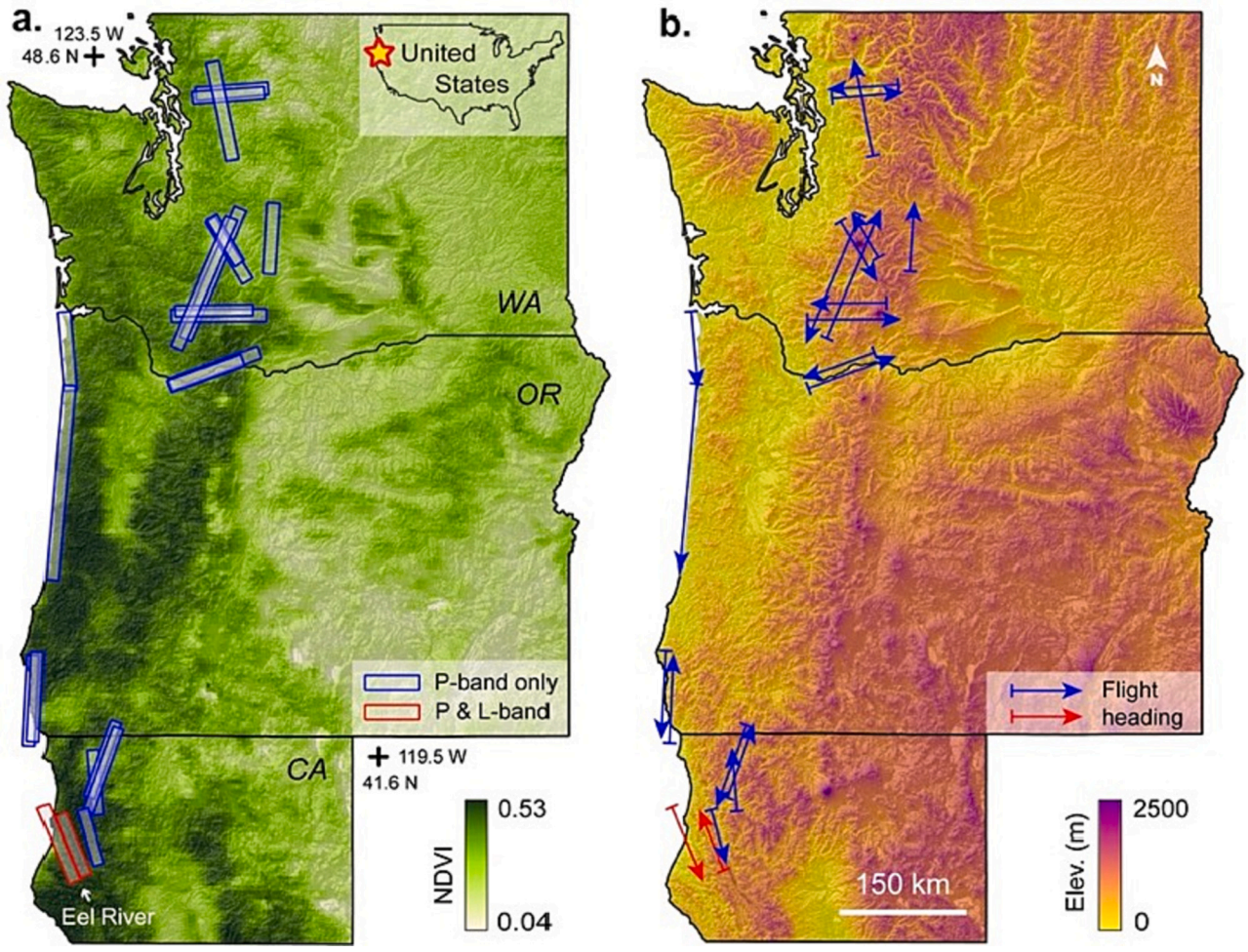

Fig. 1. Spatial coverages of the airborne P-band and L-band data. (a) Blue and red rectangular boxes depict the target areas with a background map of NDVI. The red star in the top-right corner marks the geographical location of the entire study area. (b) Blue and red arrows depict the flight direction of each data segment with a background map of elevation above sea level. The arrows are marked on the near-range side of each rectangular flight segment in commensurate colors. (For interpretation of the references to colour in this figure legend, the reader is referred to the web version of this article.)

Table 1
Parameters of P-band and L-band SAR acquisitions over the Eel River region.

Band	P-band	L-band
Side-looking direction	Left	Left
Polarization	HH	HH
Center wavelength (cm)	69.72	23.84
Bandwidth (MHz)	17.8	80
Pulse length (μs)	40	40
Average flight altitude (km)	12.5	12.5
Peak transmit power (kW)	3.1	2.0
Thermal noise equivalent σ^0 (dB)	< -50	< -40
Look angle (°)	25–55	25–65
Nominal swath width (km)	14	22
Slant range resolution (m)	8.2	1.67
Azimuth resolution (m)	0.6	0.6
Multi-looked range spacing (m)	5.0	5.0
Multi-looked azimuth spacing (m)	7.2	7.2
Dates of acquisition #1	Around 13 Nov 2020	27 Oct 2020
Dates of acquisition #2	Around 02 May 2021	13 May 2021

3. Methodology

3.1. Repeat-pass airborne SAR acquisition and InSAR processing

Repeat-track SAR interferometry from an airborne platform demands high-accuracy motion control and compensation to meet the requirements for measuring centimeter-scale earth surface deformation. Different from satellite imaging, wind gusts and turbulence in the troposphere make it difficult for an aircraft to fly the same trajectory twice, and varying crosswinds frequently alter the yaw angle leading to non-constant antenna pointing directions (Rosen et al., 2006; Rosen et al., 2000). To overcome these challenges, NASA JPL's UAVSAR radar system for both P-band and L-band utilizes a modified NASA Gulfstream III aircraft, which includes a Precision Autopilot system based on real-time DGPS (Differential GPS) and INU (inertial navigation unit) input, to control the repeat-pass flight trajectory to be within a 5 m tube (Chapin et al., 2012; Hensley et al., 2010). To minimize the yaw angle variation between repeat passes, the L-band instrument included an adjustable, electronically steered antenna to maintain a desired pointing direction based on real-time attitude angle measurements (Rosen et al., 2006); while for the P-band instrument, the same need was offset by using a much wider azimuth beamwidth of 22° compared to the 8° of L-band, which makes the P-band acquisitions more immune to yaw angle variation. The P-band and L-band instruments share the same backend electronics, thus the P-band raw and focused single-look complex (SLC) images have the same sample spacing as the L-band data but coarser range resolution. Additionally, the UAVSAR system initiates data takes automatically at appropriate locations throughout the flight based on a preset flight plan file (Chapin et al., 2012).

The generation of SLC images starts with calculating the flight trajectories of a repeat-path pair, which is achieved though blending INU and post-processed DGPS data on the ground for maximum accuracy. A subsequent motion alignment algorithm is employed to align the repeat-path data in both along-track and cross-track directions (Hensley et al., 2010). Afterwards, based on the two flight trajectories, a common coordinate system and reference path are selected to generate SLC imagery through the image formation processor. If the ephemeris knowledge were perfect, the two images would be co-registered precisely. However, currently the post processing of DGPS and INU data can only achieve a relative position accuracy of 2–15 cm (Rosen et al., 2006; Hensley et al., 2010), which is inadequate for producing high-precision InSAR results.

To achieve better image alignment, the relative position data (a.k.a. residual motion or baseline) are refined using the SLC images. These residual motions are recovered through image cross correlation by patches (approximately every 100 m in the along-track direction and 200 m in the range direction) to compute the along-track and range offsets (Madsen et al., 1993). The along-track offsets are used to estimate the residual baseline rate of change based on the formula (Hensley et al., 2009):

$$\Delta s = -b_s + b_c tan\theta_{az} + dRsin\theta_l \frac{\partial b_c}{\partial s} - R\frac{cos\theta_l}{cos\theta_{az}}\frac{\partial b_h}{\partial s} \quad (1)$$

where b_s is the along-track baseline, b_c the cross-track baseline, b_h the vertical baseline, θ_{az} the squint angle, R the range between the antenna and ground target, θ_l the look angle, s the along-track direction, and $d = 1$ for left-looking radar systems and $d = -1$ for right looking systems. A Chebyshev polynomial to the estimated baseline rates is used to smooth the estimates, which are then integrated to calculate the residual baseline (Reigber, 2001). The range offsets as a function of range are utilized to solve for the magnitude of the cross-track and vertical baselines, and then are used to determine the constants of integration for the residual baseline in the Chebyshev polynomial integration of the residual baseline rates (Rosen et al., 2006; Hensley et al., 2010). Last, the residual baseline is applied to motion files of the interferometric pair and then the data are reprocessed. Residual along-track and range offsets from the reprocessed data are used to confirm a reduction in the residual baseline. Comparisons of the corrected and uncorrected baselines of each track are accessible from the UAVSAR data portal (JPL (Jet Propulsion Laboratory), 2022).

After the residual baseline correction and a terrain-dependent motion compensation using the oversampled SRTM DEMs (Shuttle Radar Topography Mission - Digital Elevation Model) with 1-arcsecond pixel spacing, the InSAR phases of two SLC images were calculated by multiplying the complex values of one SAR image by the complex conjugate values of the other image on a pixel-by-pixel basis. We utilized a boxcar filter of 3×3 pixels to reduce speckle noise of the wrapped SAR interferograms, and we employed the ICU (integrated correlation and unwrapping) approach (Goldstein et al., 1988) to unwrap the InSAR phase by setting coherence thresholds of 0.4 for both the P-band and L-band data. Afterwards, the SAR products (i.e., SLC, coherence, and unwrapped phase) were geocoded using the oversampled SRTM DEMs (approximately 6 m × 6 m in pixel size).

Potential deformation features and geohazards (e.g., active landslides) were primarily identified from the InSAR line-of-sight (LOS) change maps, and the displacement boundaries were manually outlined, sometimes by incorporating other observations such as lidar DEMs and high-resolution optical images.

3.2. Precision of InSAR measurements

The precision of InSAR measurements is an important index that reflects the background noise level of the InSAR results. In general, ground deformation of an amount smaller than the InSAR precision is unrecognizable from the InSAR measurements, as the deformation signal would be hidden by the background noise. Here, we recall the precision of InSAR LOS measurement using the phase variance estimated from the InSAR coherence γ, which is computed as:

$$\gamma = \frac{E[u_1 u_2^*]}{\sqrt{E\left[|u_1|^2\right]E\left[|u_2|^2\right]}} \quad (2)$$

where u_1 and u_2 represent the complex values of a pixel in the two SAR images; $E[\bullet]$ denotes the expectation value, which is approximated using a sampled average within the estimation window (Just and Bamler, 1994). The analytic expression for the Cramer-Rao bound on the InSAR precision can then be estimated as (Rodriguez and Martin, 1992):

$$\sigma_d = \frac{\lambda}{4\pi}\sqrt{\frac{1}{2L}\frac{1-\gamma^2}{\gamma^2}} \quad (3)$$

where σ_d is the precision of the InSAR measurements, λ the SAR wavelength, and L the window size (in pixels) used for the coherence

estimation. The estimated phase variance is a reasonable approximation to the actual one when the window size is greater than four (Seymour and Cumming, 1994). Throughout this study, a moving estimation window of 3×12 pixels (range by azimuth) were utilized.

3.3. Resolvable spatial phase gradient of InSAR

The two-dimensional InSAR phase unwrapping relies on the assumption that the phase difference of any two adjacent pixels along the unwrapping path is less than π (Goldstein et al., 1988). Under the condition of high InSAR coherence, the maximum resolvable displacement gradient g_{max}^{los} from the radar LOS measurements can be approximated as

$$g_{max}^{los} = \frac{\lambda}{4w} \tag{4}$$

where w is the pixel spacing of the to-be-unwrapped InSAR image, and λ is the radar wavelength. Note that strong decorrelation could reduce the resolvable deformation gradients (e.g., Jiang et al., 2011). For the left-looking UAVSAR radar system, the resolvable displacement gradient g_{max}^{grd} along the ground motion direction is usually greater than g_{max}^{los} and can be derived as

$$g_{max}^{grd} = \frac{\lambda}{4w(\boldsymbol{l} \bullet \boldsymbol{s}^T)} \tag{5}$$

where $\boldsymbol{l} = [-\sin\theta_{inc}\cos\phi_{head} - \sin\theta_{inc}\sin\phi_{head} - \cos\theta_{inc}]$ and $\boldsymbol{s} = [\cos\alpha_{slp}\sin\beta_{asp}\ \cos\alpha_{slp}\cos\beta_{asp} - \sin\alpha_{slp}]$ are the unit vectors along the radar LOS and ground movement directions, respectively, in a three-dimensional geographical coordinate system composed of east (E), north (N), and zenith (Z) components (Fig. 2). θ_{inc} is the incidence angle of the radar sensor, ϕ_{head} the flight heading angle (clockwise from north as positive), and α_{dip} the dip angle and β_{asp} the aspect (clockwise from north as positive) of the ground motion vector $\boldsymbol{s}$, respectively (e.g., Cascini et al., 2010).

As described by eq. (5), the maximum resolvable InSAR phase gradient differs, depending on the radar wavelength, the pixel size of the SAR image, and the LOS direction of the radar sensor. Consequently, the UAVSAR P-band's left-looking design, variable heading angles and incidence angles, and the achievable pixel resolutions, determine its unique capability for resolving ground displacement.

3.4. Radar penetration depth

Effective InSAR measurements demand repeat-pass SAR acquisitions to contain coherent backscattering signals. The Earth's surface materials (i.e., SAR scatterer) are subject to frequent changes by seasonal precipitation, snowfall, erosion, and other surficial processes. By contrast, more stable backscatter tends to exist within the subsurface layers, into which long-wavelength radars can penetrate. The electromagnetic penetration depth of radars is defined as the depth where the amplitude of the electromagnetic radiation strength in a medium falls to $1/e$ of its original value. In a homogenous medium of dielectric constant $\varepsilon = \varepsilon' - j\varepsilon''$, the penetration depth δ_p is given by (Ulaby et al., 1982):

$$\delta_p = \frac{\lambda}{4\pi}\left\{\frac{\varepsilon'}{2}\left[\sqrt{1+\left(\frac{\varepsilon''}{\varepsilon'}\right)^2} - 1\right]\right\}^{-\frac{1}{2}} \tag{6}$$

where λ is the radar wavelength. The real part of the complex dielectric constant ε' is associated with the stored energy when the substance is exposed to an electromagnetic field, and the imaginary part ε'' is the loss factor, which affects energy absorption. As indicated by eq. (6), the P-band SAR penetrates much deeper than L-band in the same media owing to its longer wavelength. For the side-looking SAR, the vertical penetration depth can be approximated as $\delta_p' = \delta_p \cos\theta_{inc}$ using Snell's law when $\varepsilon'' \ll \varepsilon'$(e.g., Singh et al., 2018).

The dielectric property of natural soils, which are composed of solid soil particles and water, is strongly dependent on the soil type and moisture content (Dobson et al., 1985). For example, at moisture content of 5%, field measurements reported an averaged dielectric constant of $\varepsilon_{soil} = 5 - j0.5$ for various soil types. However, both ε' and ε'' increase with soil moisture, indicating a reduction in radar penetration depth (Peplinski et al., 1995; Hallikainen et al., 1985). Field measurements show that saturated soils may contain up to 50% of water depending on soil type (USDA, 2022).

The dielectric properties of wet snow, ε_{ws}' and ε_{ws}'', similarly vary by water content and can be estimated as (Tiuri et al., 1984): $\varepsilon_{ws}' = \varepsilon_{ds}' + \Delta\varepsilon_s' = 1 + 1.7\rho_d + 0.7\rho_d^2 + (0.1p_w + 0.8p_w^2)\varepsilon_w'$ and $\varepsilon_{ws}'' = (0.1p_w + 0.8p_w^2)\varepsilon_w''$, where ρ_d is the dry density of snow relative to water, p_w the volumetric water content, and $\varepsilon_w = \varepsilon_w' - j\varepsilon_w''$ the complex permittivity of water ($\varepsilon_w = 88 - j9.8$ at radar frequency of 1 GHz). Field measurements of moist snow (p_w= 0.014) at Lionhead Mountain, Montana (USA) yielded an average value of $\bar{\varepsilon}_{ws} = 1.51 - j0.015$ (Bradford et al., 2009), which matches the theoretical estimation of ε_{ws}=1.66 − j0.015.

4. Overview of ground deformation mapped from P-band InSAR

Utilizing the 22 segments of repeat-pass P-band SAR data that we acquired over distributed areas on the U.S. West Coast, we produced commensurate deformation maps through the InSAR technique to identify localized ground deformation (e.g., active landslides) between 13 November 2020 and 02 May 2021 (Fig. 3). Moreover, we compared these identified deformation features (predominantly slow-moving landslides) with the USGS (U.S. Geological Survey) landslide inventory (Jones et al., 2019) and the landslide database generated from 2007 to 2019 ALOS/ALOS-2 (Advanced Land Observing Satellite) L-band InSAR observations (Xu et al., 2021b).

In total, we identified 257 active landslides during the observation

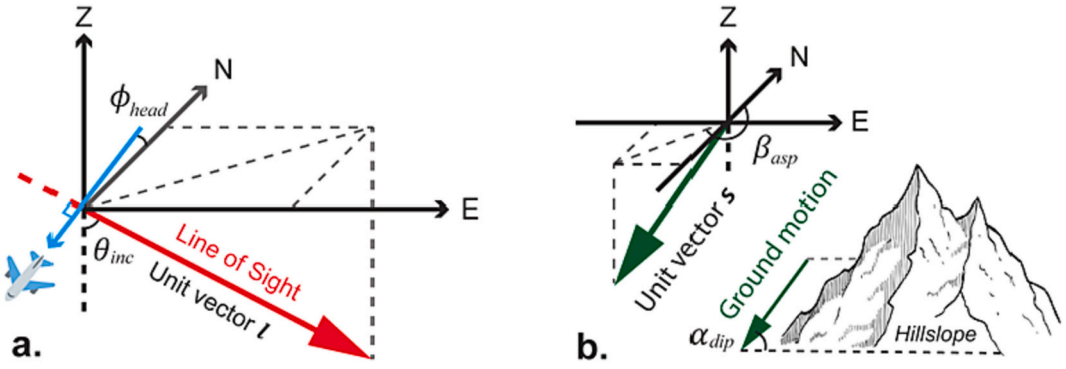

Fig. 2. Projection of one-dimensional ground deformation to SAR LOS direction. (a) Decomposition of a radar LOS vector and (b) an exemplary downslope movement vector.

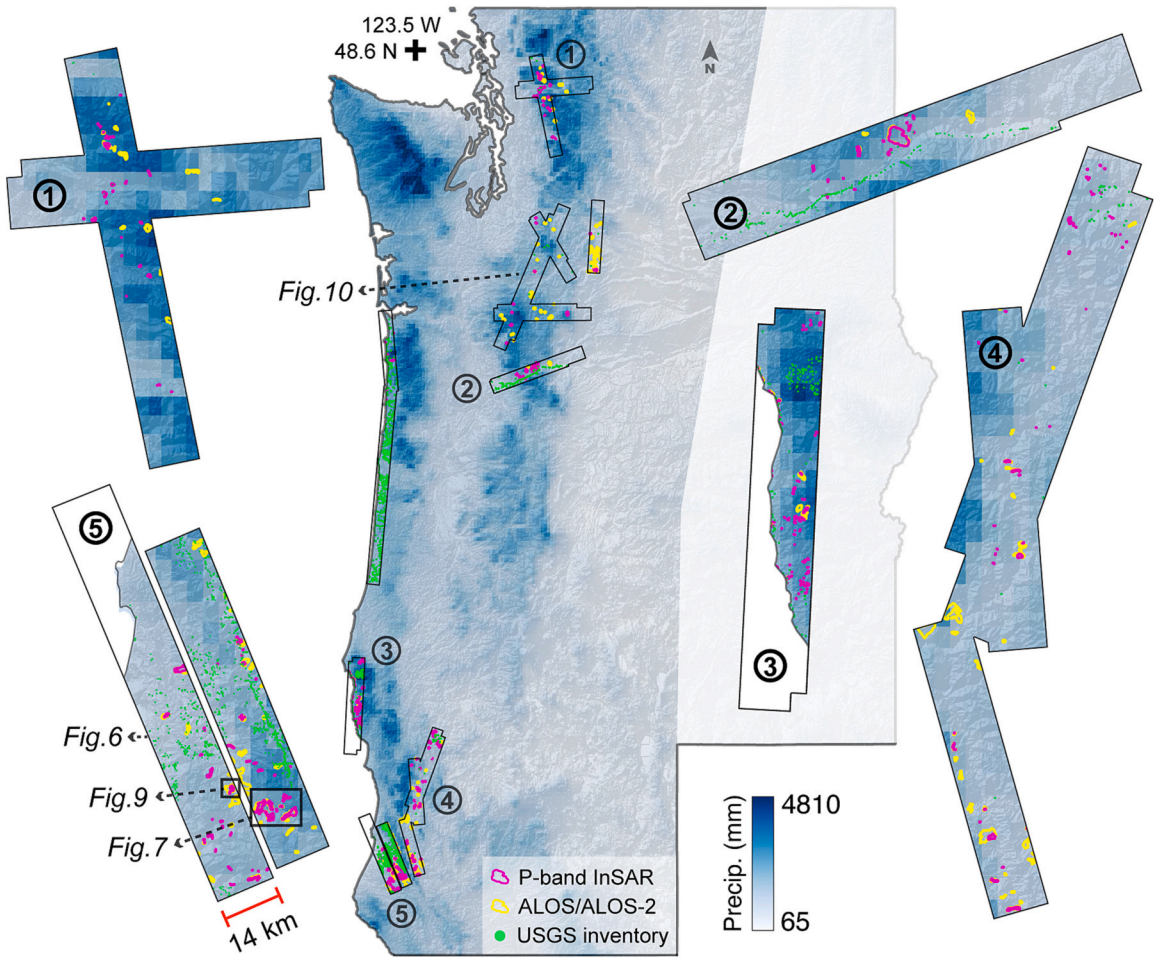

Fig. 3. Mapped landslides from P-band InSAR and a comparison to the USGS landslide inventory (Jones et al., 2019) and the 2007–2019 ALOS/ALOS-2 InSAR identifications (Xu et al., 2021b). The background map was produced from the 1981–2010 average precipitation (PRISM Climate Group, 2022). Five selected areas (#1 - #5) are shown in scaled-up sub-panels.

period using the P-band InSAR, of which 231 were missing from the USGS landslide inventory, and 195 were not reported from the 2007–2019 L-band ALOS/ALOS-2 InSAR observations (Fig. 3). The dimensions of the mapped landslides range from 3.7×10^3 to 12×10^6 m^2. The slow motion of these landslides indicate that they are already in a state of force imbalance, so are potential candidates for a future disaster under the disturbance of earthquakes, intense rainfall, and/or anthropogenic activities (Lacroix et al., 2020).

Many of the identified landslides were missing from the USGS inventory, potentially because the USGS landslide inventory was primarily based on geological maps and human reports, so the slowing-moving landslides without obvious geomorphic signatures (e.g., headscarps) or located in remote forests were less likely to be reported (e.g., Xu et al., 2021b). Some of the identified landslides were also missing from the L-band ALOS/ALOS-2 InSAR results, which can be primarily attributed to two causes. First, the airborne SAR has relatively finer pixel spacings than the satellite ALOS/ALOS-2 data to allow for identifying small-sized landslides: airborne P-band SAR of 1.67 m × 0.6 m (range by azimuth) versus satellite ALOS-2 of 4.3 m × 3.2 m (e.g., Xu et al., 2021a). Second, the P-band SAR has a stronger capability to penetrate through dense forests to achieve better InSAR coherence (detailed in Section 5.2).

The comparison results also revealed that the 1932–2017 USGS landslide inventory includes considerably more landslides than our P-band InSAR identifications in particular regions, such as the central Oregon coast, the Columbia River area in southern Washington (Area #2 in Fig. 3), and the Eel River region in northern California (Area #5 in Fig. 3). This could be because the USGS inventory included many onetime landslides, which were no longer active between November 2020 and May 2021. Alternatively, some might be catastrophic landslides, which induced severe coherence loss to render InSAR measurements ineffective. In addition, 87 landslides were found to be active by the 2007–2019 ALOS/ALOS-2 InSAR observations, yet they were missing from the P-band InSAR identifications. The potential causes include these landslides' inactivity from November 2020 to May 2021, P-band SAR's insensitivity to subtle deformation (detailed in Section 5.5), and/or the different look angles between satellite and airborne SAR sensors.

5. Evaluation of P-band versus L-band SAR - Eel River region

Over the Eel River region (Figs. 1 & 4), we acquired both P-band and L-band data with identical flight heading and similar look angle around the same dates (Table 1) to allow for a comparison of P and L-band SAR. Two flight segments with opposite headings were collected for each band (Fig. 1): flying southeast for the western segment, and northwest for the eastern segement. These two flight segment areas are dominantly covered by evergreen forest (64%), followed by mixed forest (9%), developed open space (6%), grassland and herbaceous land (6%), shrub/scrub (5%), shrub forest (4%), deciduous forest (3%), and other land types (Fig. 4; Yang et al., 2018). In comparison, the western segment covers more developed space, open water, and pasture/hay landtypes near a coastal town than the eastern one (13% versus none), while the eastern segment covers more herbaceous/shrub forests than the western one (7.6% versus 1.9%). Detailed comparisons between the

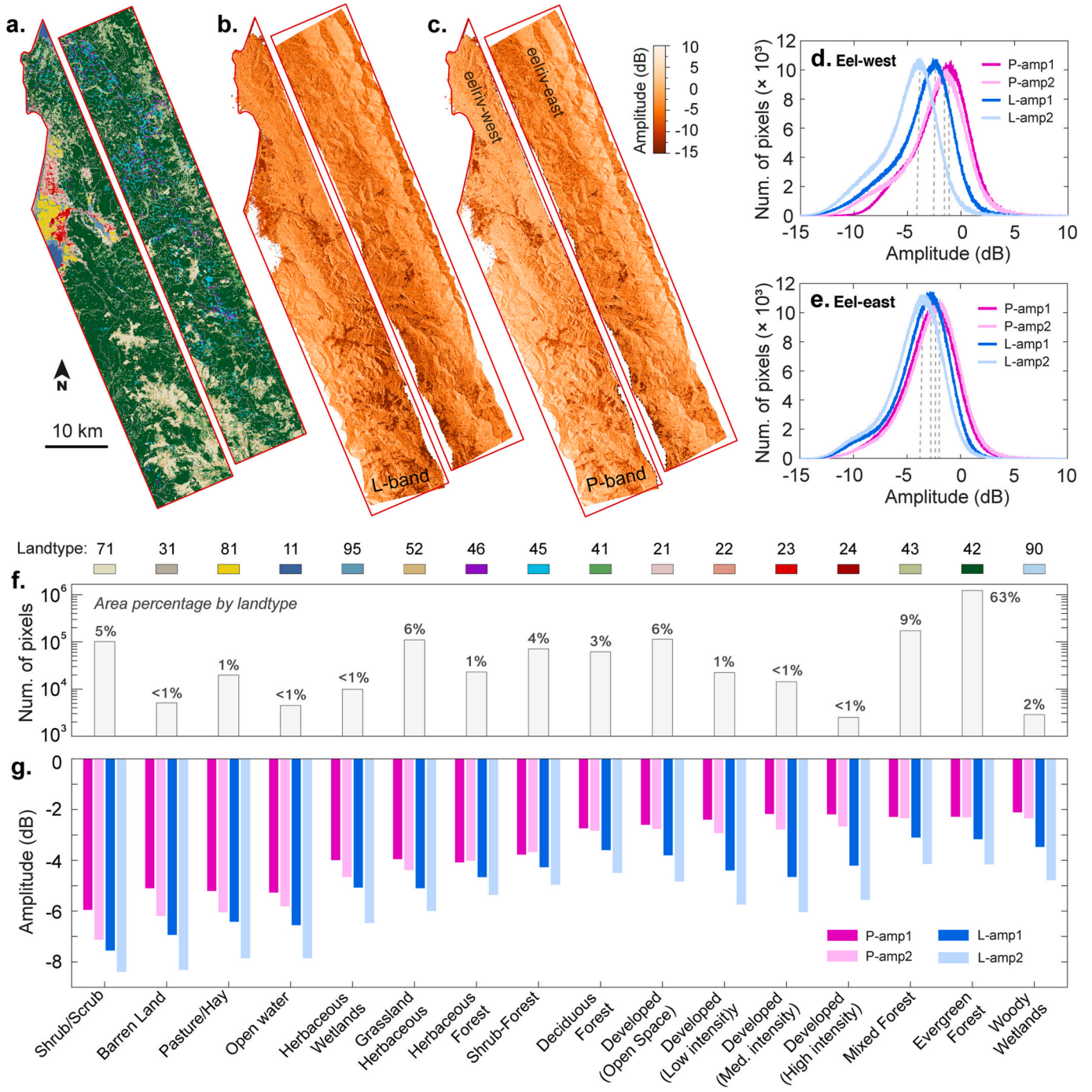

Fig. 4. Comparison of post-calibration backscattering amplitude of the HH-polarization P-band and L-band SAR over the Eel River region. (a) illustrates land cover types based on the classifications and colormaps in Yang et al. (2018), with a legend given immediately above Fig. 4f. (b) and (c) compare backscattering amplitudes of the first L-band (27 Oct 2020) and P-band acquisitions (13 Nov 2020), respectively. (d) and (e) show the amplitude probability distribution of the first and the second P/L-band acquisitions for the western and eastern flight segments, respectively. Here, the first/s P-band acquisition is annotated as "P-amp1/2". (f) depicts the pixel counts (in logarithmical scale) and area percentages of each land type in the entire Eel River region. (g) shows the comparison of backscattering amplitude for variable land cover types.

P-band and L-band SAR regarding the backscattering amplitude, InSAR coherence, quality of InSAR measurements, ability to measure spatially high-gradient displacement, and sensitivity to subtle deformation are presented below.

5.1. Backscattering amplitude

Fig. 4 shows that the P-band SAR received slightly stronger backscattering amplitudes than the L-band SAR by 1.65 dB on average over the entire Eel River region. The amplitude medians suggest a similar trend (Fig. 4d,e), with the western flight segment showing more significant difference (1.85 dB) than the eastern flight segment (0.85 dB) between the P and L bands. The amplitude median of SAR data usually varies within 0.5 dB depending on the acquisition date, but an exception of 1.7 dB was found for the L-band acquisitions on the western segment. Technically, the amplitude differences between the P-band and L-band

SAR result are dominated by surface roughness effects and partly from soil moisture m_v (Lu and Meyer, 2002). An empirical relationship can be given as (Zribi and Dechambre, 2003): $\sigma^0_{dB} = am_v + be^{-kh_{rms}} + c$, where σ^0_{dB} is the backscattering coefficient in decibels, $k = 2\pi/\lambda$ is the wave number, h_{rms} is root-mean-square surface height, and the coefficients a, b, and c are dependent on both radar incidence angle and polarization. In general, the SAR backscattering amplitude correlates positively with radar wavelength and soil moisture. Note that soil moisture may vary by season and following recent rainfall events. The first and second SAR images were collected in November 2020 (wet winter season) and May 2021 (dry summer season), respectively.

In general, areas with tall vegetation (e.g., forests) showed much greater backscattering amplitude for both P-band (> -4 dB) and L-band (> -5 dB) SAR, owing to the stronger volume scattering (Fig. 4g). By contrast, areas with short vegetation and barren lands showed much lower SAR amplitude (< -4 dB for P-band and < -5 dB for L-band). Interestingly, developed areas, ranging from low intensity to high intensity, all manifested significant amplitude differences between P and L-band SAR acquisitions by 2.4 to 2.9 dB (Fig. 5). Large amplitude differences were also found for barren land (2.0 dB), woody wetlands (1.9 dB), open water (1.67 dB), and developed open space (1.64 dB) (Fig. 5a). The amplitude difference in the bare-surface areas between the P and L-band acquisitions can be attributed to ground cover differences, from emergent grasses or other small vegetation between May and November. Phenology impact of trees in developed spaces could also cause seasonal backscatters and lead to different response in P and L bands.

5.2. Coherence of repeat-pass SAR acquisitions

When using InSAR to survey ground deformation, the coherence of repeat-pass acquisitions is a critical and straightforward measure to evaluate the potential precision of InSAR measurements, as shown in eq. (3). Over the Eel River region, Fig. 6 shows that the P-band SAR maintained much better coherence than the L-band acquisitions. For both the western and eastern flight segments, P-band InSAR had a coherence median of approximately 0.7, in comparison to the much lower 0.4 for L-band data (Fig. 6d,e).

Not surprisingly, the InSAR coherence of both P and L-band acquisitions is strongly dependent on land cover types (Fig. 6f). In general, both bands retained relatively good coherence for developed spaces and herbaceous forest, with coherence >0.55 for P-band and > 0.43 for L-band. By contrast, much lower coherences were encountered over herbaceous wetlands and pasture/hay for both the P (< 0.36) and L (<0.23) bands. More interestingly, P-band SAR showed significantly higher coherence than the L-band data (coherence difference > 0.17) over woody wetlands (0.2), mixed forest (0.19), evergreen forest (0.17), developed open space (0.17), and developed space with low intensity (0.17) (Fig. 5b). Note that the mixed forest and evergreen forest together constitute 72% of the Eel River region (Fig. 4f).

The coherence difference of P/L-band InSAR lies primarily in radar's wavelength-dependent penetration capability. In the forested areas, the long-wavelength P-band SAR is more capable of penetrating through dense forest canopies to collect relatively coherent signals from the ground surface, which are stronger than the returns from tree leaves and branches that are subject to wind motion and seasonal growth. In the regions with sparse vegetation or bare surface, P-band SAR can penetrate to much deeper subsurface layers than the L-band, where the soil composition and moisture content are relatively steady throughout the year on the U.S. west coast (e.g., USDA, 2022; Xu et al., 2019). In contrast, surface layers contain less steady scatterers, owing to material alteration by surficial processes (e.g., vegetation growth and surficial erosion) and soil moisture fluctuation by seasonal precipitation (e.g., USDA, 2022). Using the dielectric constant of $\varepsilon_{soil} = 5 - j0.5$ for moist soils (Peplinski et al., 1995; Hallikainen et al., 1985) and eq. (6), we can estimate that P-band SAR collects backscattering signals from a depth down to 0.5 m beneath the bare surface (along the LOS direction), in comparison to 0.17 m for the L-band. This greater penetration depth partly helped P-band SAR data to maintain higher coherence. Additionally, the longer-wavelength P-band SAR experiences less volume decorrelation than the L-band while penetrating into the media (Hoen and Zebker, 2000).

5.3. Quality of SAR interferometry

To have a clear illustration of the capabilities of P-band and L-band InSAR for discovering ground displacement, we highlight a small landslide-prone area within the Eel River region for a comparison (Fig. 7). The geographical location of this highlighted area is outlined in Figs. 3 & 6a. As shown in Fig. 7, the P-band SAR interferogram captured the landslide deformation more clearly than the L-band, as indicated by

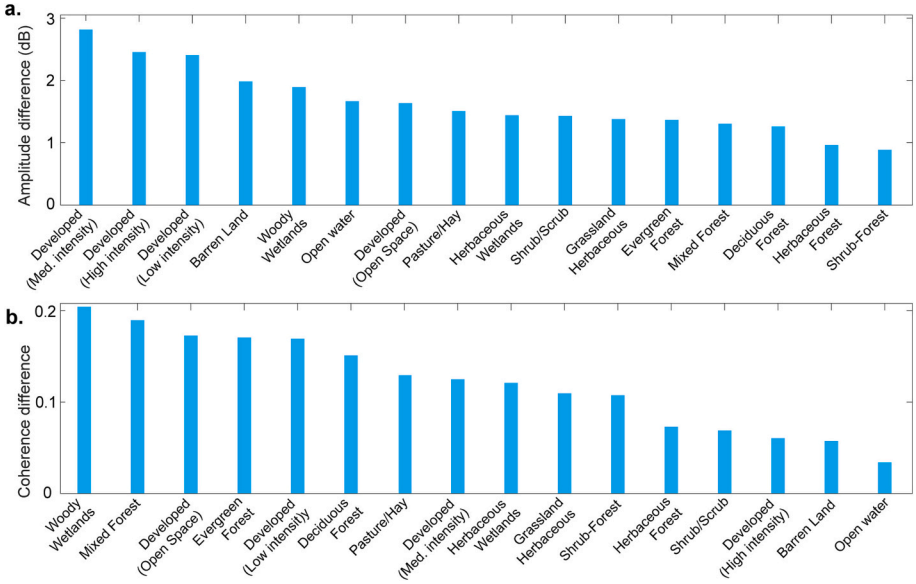

Fig. 5. Amplitude and coherence differences in P and L bands over the Eel River region. (a) Amplitude differences of the P versus L-band SAR by land cover type. The averaged amplitude of the November 2020 and May 2021 acquisitions were used to calculate the difference. (b) Coherence differences of P- and L-band InSAR by land cover type.

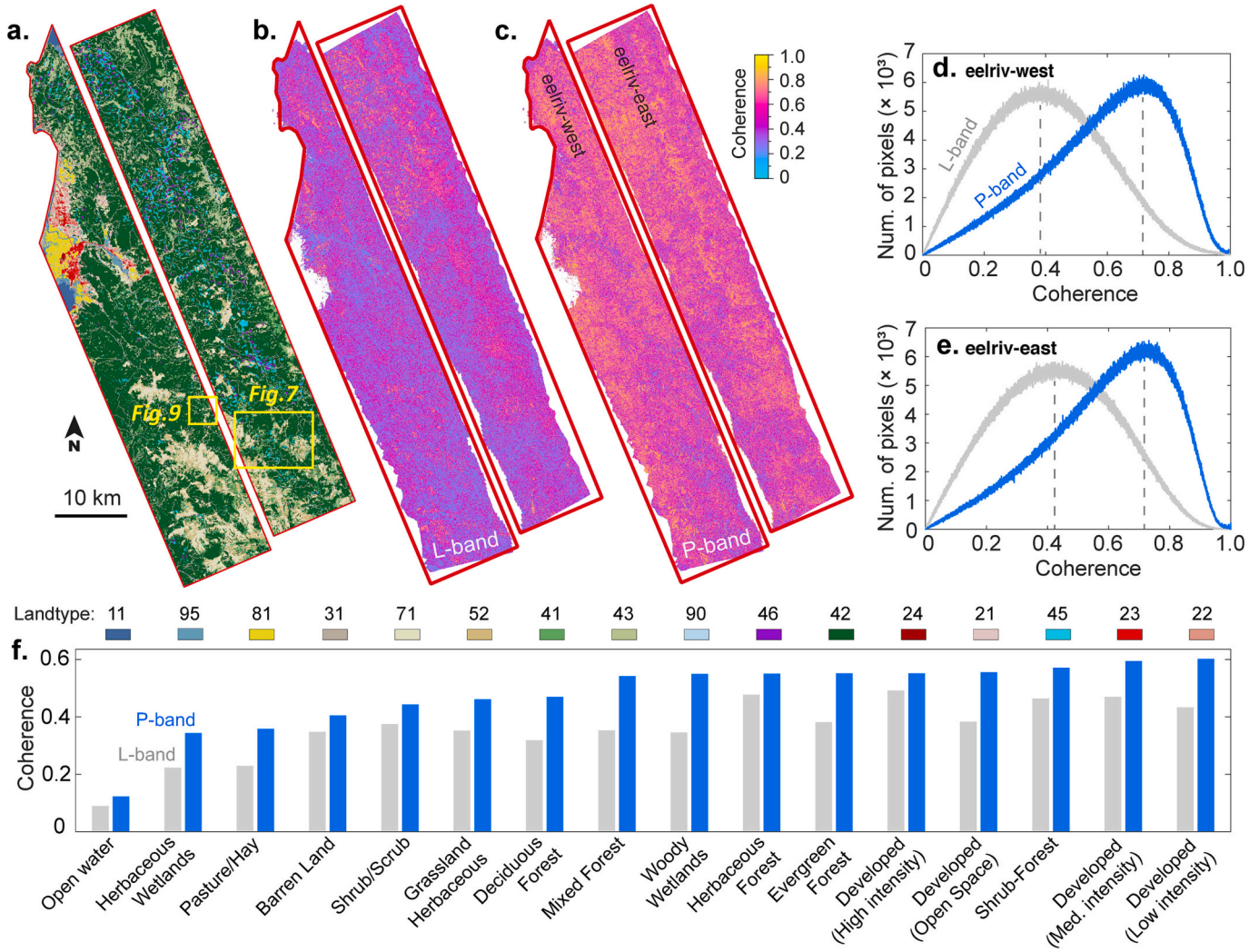

Fig. 6. Comparison of coherence of P-band and L-band InSAR. (a) shows the land cover type with a legend given immediately above Fig. 6f. (b) and (c) depict InSAR coherence of L-band and P-band data, respectively. (d) and (e) compare coherence probability distribution of the P/L-band InSAR for the western and eastern flight segments, respectively. (f) shows the average P/L-band InSAR coherence for each land cover type.

a much lower level of background noise. This is of critical importance to accurately determine landslide boundaries. In terms of InSAR coherence, the P-band SAR also performed much better with coherences >0.5, in comparison to <0.4 for one thirds of the area from the L-band SAR (Fig. 7c,d). In unwrapped interferograms, P-band InSAR outperformed the L-band regarding the number of measurable unwrapped points, which is a key to capturing the spatial pattern of landslide dynamics. In summary, P-band InSAR overall demonstrated better quality for detecting ground deformation in this vegetated area.

As explained in Section 5.2, P-band SAR's stronger capability of penetrating through dense forests and surface soils was most likely the cause for its better performance than the L-band SAR. Such advantages are particularly prominent over densely forested regions, but less significant over areas without much vegetation (Figs. 7 & 8). Note that P-band SAR may also encounter coherence loss and phase unwrapping difficulties owing to highly dense vegetation and large deformation (Fig. 7e).

5.4. Measurement of spatially high-gradient displacement

Given a particular pixel size that is determined by the SAR instrument, measuring spatially high-gradient surface displacements is one of the primary challenges that InSAR frequently encounters in studies of non-tectonic and tectonic deformation processes. Typical examples include ground subsidence caused by underground mining (e.g., Wang et al., 2018), slow-moving landslides (e.g., Handwerger et al., 2015), and concentrated fault ruptures (e.g., Li et al., 2011), where high-gradient displacements often lead to unresolvable phase jumps for short-wavelength InSAR. Here, we highlight an example of the slow-moving Cameron Ridge landslide (Fig. 8) to showcase P-band SAR's capability for measuring spatially high-gradient deformation.

Fig. 8b shows that the Cameron Ridge landslide only has sparse and shallow vegetation (i.e., predominantly grassland and herbaceous plants), which indicates that the significant decorrelation of L-band InSAR within the landslide area can be primarily attributed to landslide motion. In comparison, the masked-out low-coherence areas (coherence <0.4), which are located west and immediate south of the landslide on the unwrapped L-band interferogram (Fig. 8c), are more likely caused by dense vegetation (see Fig. 8b). As shown in Fig. 8d, at the upper section of the landslide along the longitudinal profile *A*-*A*′, the landslide displacements were gradual (i.e., low spatial displacement gradient) and were measurable by both the P and L-band InSAR. Moving downslope to about 1500 m distance from point *A*, high displacement gradients were encountered, which appear as a decorrelated area in the L-band SAR interferograms (Fig. 8c) leading to unresolvable phases (i.e., the masked-out area of coherence <0.4). By contrast, the longer-wavelength

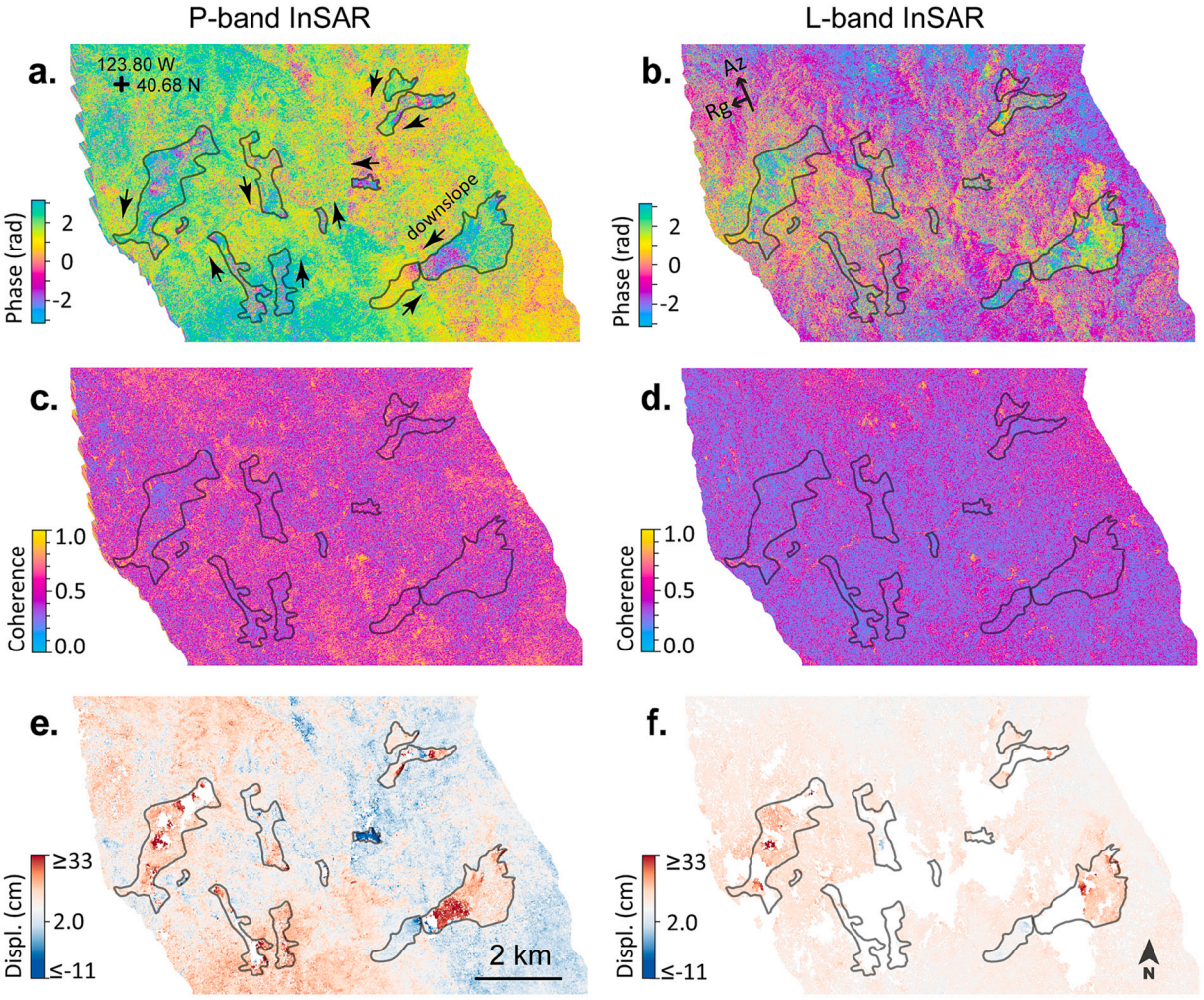

Fig. 7. Comparison of P-band and L-band InSAR for detecting localized deformation over vegetated terrains. (a), (c), and (e) show the wrapped interferogram, coherence map, and unwrapped interferograms derived from the P-band SAR images, respectively. (b), (d), and (f) show the corresponding results derived from the L-band images. The black arrows in (a) denote the average downslope directions of the landslides (generally towards the creek as visible in Fig. 8b). Blank spaces in (e) and (f) are masked-out areas during phase unwrapping using a coherence threshold of 0.4.

P-band InSAR could resolve the displacements in this section successfully, because a phase of π (potentially a phase jump) in L-band InSAR only corresponds a phase of $\pi/2.9$ on P-band data owing to the ratio of the wavelengths. Moving further downslope to the landslide toe area, both the P-band and L-band InSAR encounter difficulties resolving the displacements, potentially owing to the very high displacement gradients.

Along the transverse direction from B to B', high displacement gradients were encountered throughout the profile for the L-band InSAR (Fig. 7e), thus only the P-band InSAR was able to quantify the deformation. However, the very high displacement gradients near the landslide boundaries were also unresolvable by the P-band data. From eq. (5) we can see that, with identical flight path and side-looking angle, the P-band SAR can resolve displacement gradients that are 2.9 times as high as those resolved by the L-band SAR, due to the advantage of a longer radar wavelength.

5.5. Sensitivity to subtle deformation

In contrast to high-gradient displacements, recognition of subtle, low-amplitude deformation demands a low background noise to allow deformation signals to be clearly distinguishable. As shown in eq. (3), both radar wavelength and InSAR coherence impact the background noise level (i.e., InSAR precision). Here, we highlight the slowly moving Graham Creek landslide as an example to compare P-band and L-band InSAR's abilities to capture subtle deformation features (Fig. 9). The geographical location of this landslide was shown in Figs. 3 and 6a.

Fig. 9 shows that both the P-band and L-band interferograms detect deformation signals over the Graham Creek landslide complex. Excluding the masked-out areas (InSAR coherence <0.4), P-band SAR was able to retain an average coherence of 0.7, much higher than the L-band InSAR of 0.45. However, on the unwrapped interferograms, the "recognizable" deformation areas from the P-band SAR are much smaller than those from the L-band SAR (Fig. 9). Only the three relatively fast-moving sections within the landslide complex were distinguishable from the P-band observations, whereas other sections were hidden by the background noise. By contrast, the L-band InSAR was able to reveal a much larger deforming body of the landslide complex (Fig. 9). However, the fast-moving northeast and southmost sections, which potentially caused substantial decorrelation for the L-band InSAR, were only measurable by the P-band InSAR.

Using eq. (3), we can obtain that the achievable precision of InSAR measurement from P-band SAR was 0.28 cm, whereas that from L-band InSAR was 0.18 cm. Consequently, despite of the higher coherence, P-band InSAR is relatively less sensitive to subtle deformation than L-band InSAR in certain environmental settings.

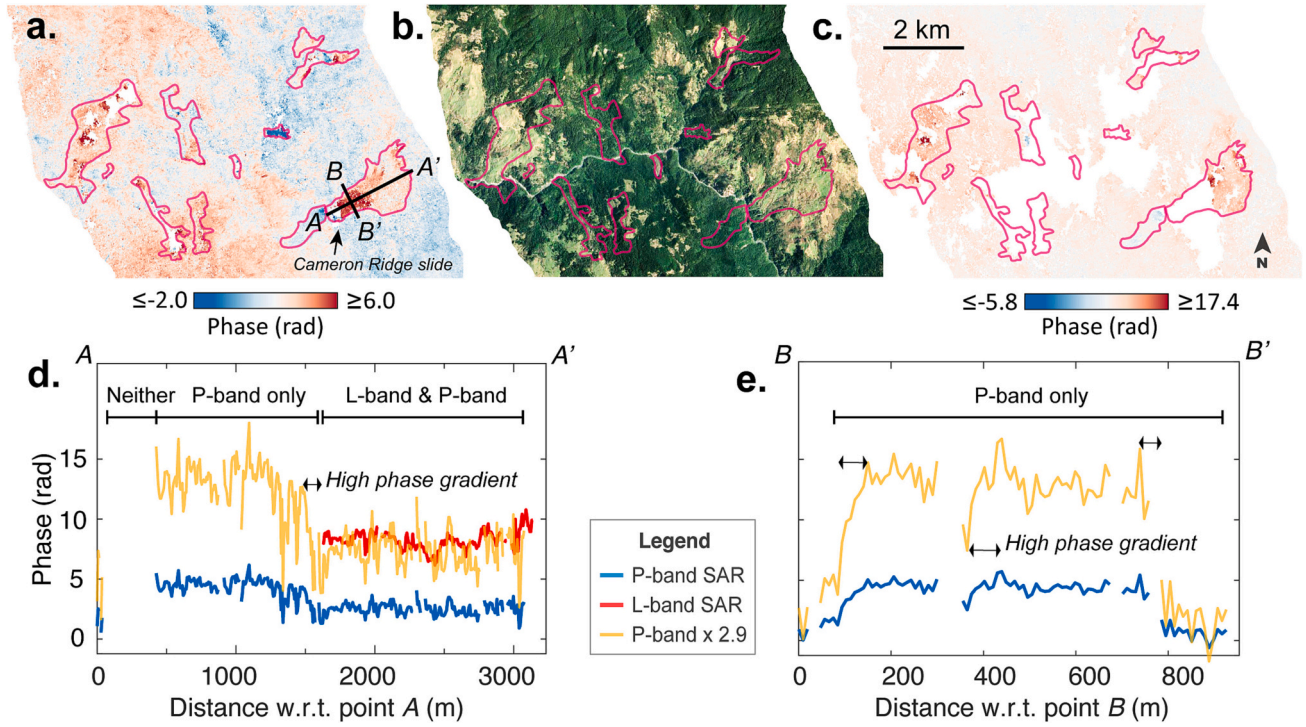

Fig. 8. Capability of P-band and L-band InSAR for measuring high-gradient deformation. (a) and (c) depict the unwrapped P-band and L-band interferograms, respectively. (b) April 2019 optical image of the same area. (d) shows the measured unwrapped phase of the landslide displacement along the longitudinal profile *A*–*A'* in (a), and (e) shows the measured phases along the transverse profile *B*–*B'*. The legend "P-band× 2.9" means converting P-band phase to equivalent L-band phase.

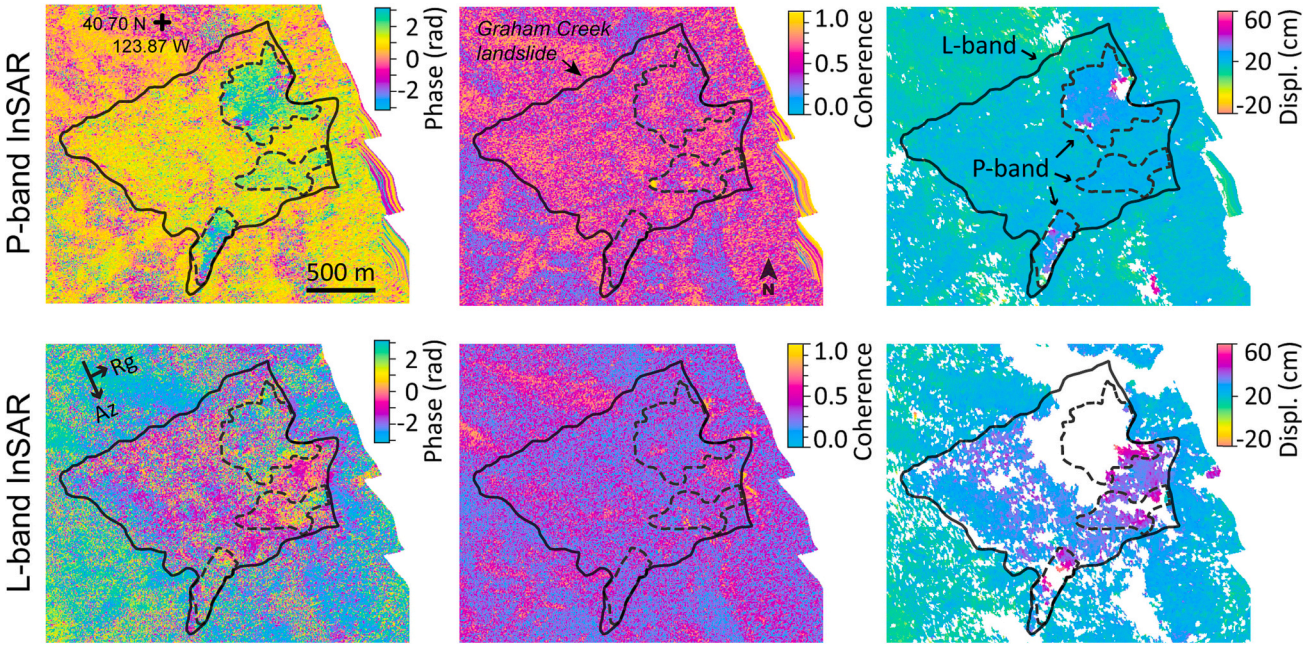

Fig. 9. Sensitivity of P-band and L-band InSAR to subtle ground deformation. The top three panels are wrapped interferogram, coherence map, and unwrapped interferogram from the P-band InSAR, respectively. The bottom three panels are corresponding images from the L-band InSAR. The dashed and solid polylines denote landslide boundaries inferred from the P-band and L-band InSAR, respectively. The blank spots on the unwrapped interferograms are masked-out areas (coherence <0.4).

6. Evaluation of snow penetration capability - Cascade mountains

Seasonal snowfall and melting, which determine snowpack thickness and surface features, are another challenge for short-wavelength SAR to achieve high coherence and thus desirable InSAR measurements. We investigated P-band InSAR's performance over snow-covered terrains, by using repeat-pass acquisitions covering three of the high mountain areas (i.e., Mt. Rainier, Mt. St. Helens, and Mt. Adams) in the Cascade Ranges (Fig. 10), the NGSA (National Gridded Snowfall Analysis) snow

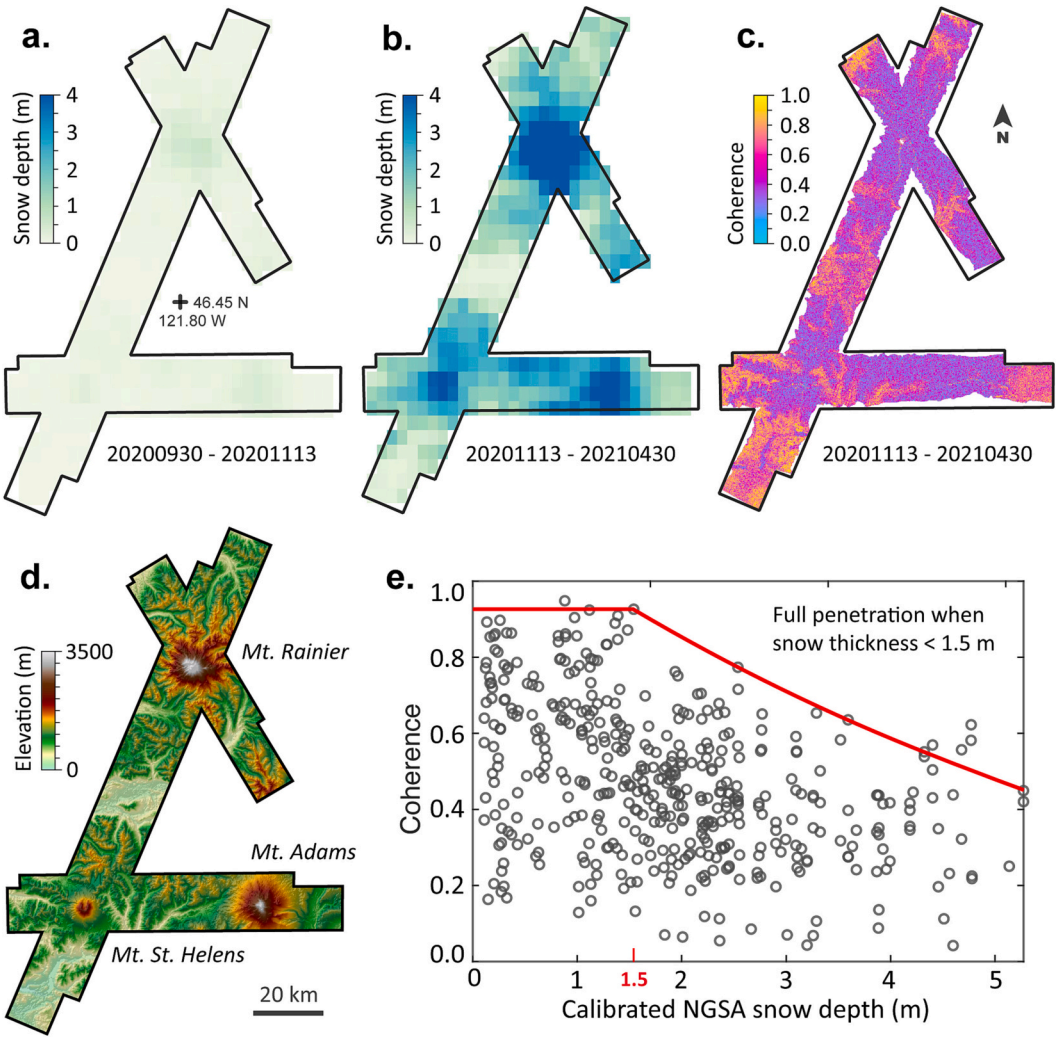

Fig. 10. Performance of P-band InSAR over snow-covered terrains. (a) and (b) depict the snow depth changes during 20,200,903–20,201,113 (YYYYMMDD) and 20,201,113–20,210,430, respectively, using the calibrated NGSA data. (c) shows coherence map of the P-band InSAR pair 20,201,113–20,210,430. (d) illustrates elevations of the area. (e) shows a scatter plot of InSAR coherence and snow depth from 20,201,113 to 20,210,430. A qualitative, piecewise trend line is shown in red. (For interpretation of the references to colour in this figure legend, the reader is referred to the web version of this article.)

depth data (NWS (National Weather Service), 2022), and daily snow depth measurements at 23 SNOTEL (snow telemetry) stations (Fig. 11).

The NGSA data in 0.04° × 0.04° resolution record the cumulative snow depths based on daily snowfall, and therefore are not a direct measure of snowpack thickness. To obtain snowpack thickness data covering the entire study area, we utilized daily snow depth measurements at 23 SNOTEL stations (USDA, 2022) from 13 November 2020 to 30 April 2021 to calibrate the NGSA data. Geographical locations of these SNOTEL stations are shown in Fig. 11a. A linear relationship of $d_s = 0.38d_n - 0.59$ (R^2=0.76) was found between the SNOTEL observations d_s and the NGSA records d_n (Fig. 11b), and was used to compute the calibrated NGSA snow depth.

By incorporating the calibrated snow depths, we found that change of snowpack thickness between the first and the second SAR acquisitions had significant impact on the InSAR coherence (Fig. 10b,c). Severe coherence loss (coherence <0.3) was observed at and near the three volcanic mountains, where maximum change of snow depth exceeded 3 m owing to the high elevation. By contrast, the areas with relatively shallow snowpacks (i.e., snow depth < 0.5 m) could retain coherences higher than 0.7. A scatter plot containing all of the observation pixels (Fig. 10e) shows that, in general, the InSAR coherence was relatively unaffected by the change of snowpack thickness on the two acquisition dates, if the change was within 1.5 m. For example, many pixels with snow depth ranging from 0 to 1.5 m could maintain coherences as high as 0.9 (Fig. 10e). However, once the snowpack thickness exceeded 1.5 m, the InSAR coherence generally decreased with snow depth, as revealed by the decreasing highest coherence (Fig. 10e).

The ground surface was barely covered by snow during the first SAR acquisition on 13 November 2020 (Fig. 10a), while during the second SAR acquisition on 30 April 2021, the ground surface was covered by snowpack ranging from 0 to 5.3 m thick (Fig. 10b). P-band SAR was able to collect coherent data despite such alteration of surficial scatterers (e.g., in the areas surrounding Mt. St. Helens and Mt. Rainier (Fig. 10c)), because the P-band radar could penetrate through shallow snowpack to collect backscattering signal from the soils beneath. However, once reaching the earth surface (i.e., soils), radar can penetrate through wet soils by only limited depth (discussed in Section 5.2). Using eq. (6) and an averaged complex dielectric constant of $\varepsilon = 1.56 - j0.015$ for slightly moist snow (volumetric water content ≈ 0.014) measured in Montana, USA (Bradford et al., 2009), we can estimate that the P-band SAR can penetrate through moist snowpack by approximately 9.2 m. It is equivalent to 7.1 m in vertical depth considering the radar's average incidence angle of 40°. The radar penetration depth of snow decreases rapidly with water content. Following the theoretical approximation detailed in Section 3.4, we can estimate a dielectric constant of $\varepsilon = 2.3 - j0.009$ for wet snow (p_w= 0.06), which corresponds to a vertical radar

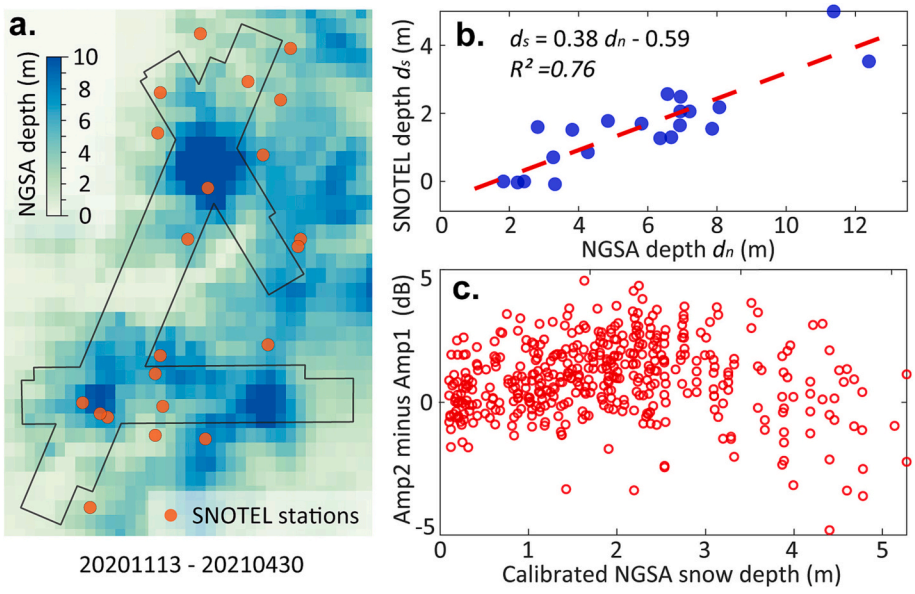

Fig. 11. Calibration of NGSA snow depths. (a) The NGSA snow depth change from 13 November 2020 to 30 April 2021 and geographical locations of the SNOTEL stations. (b) A linear fitting of the NGSA and SNOTEL snow depths. (c) The relationship between snow depth changes and SAR amplitude changes.

penetration depth of 1.43 m and has a better match with the InSAR-inferred penetration depth of 1.5 m. Note that snowpack wetness generally ranges from 0 to 15% in the field (Techel and Pielmeier, 2011), but we did not have direct measurements of snow wetness in the Cascade mountains. Additionally, we found that the SAR amplitude increased with snowpack thickness until the snow reaches 2.5 m thick, whereafter a negative correlation was observed (Fig. 11c). The relationship between SAR amplitude difference and InSAR coherence, however, seemed to be random. The wrapped InSAR phase also does not exhibit clear correlation with snow depth.

To summarize, high InSAR coherences were found in areas where snowpack thickness changed by <1.5 m, potentially because P-band radar could penetrate through the snow cover to collect backscattering signals from the ground surface. However, over areas with moist and thick snowpack (> 1.5 m), P-band InSAR started to experience increasingly stronger coherence loss. Note that the radar penetration depth can increase significantly for dry ice and snow. For example, the C-band SAR was reported to reach a penetration depth of 12 to 35 m for the Greenland Ice Sheet (Hoen and Zebker, 2000). P-band radars are expected to achieve even greater penetration depth under similar conditions.

7. Discussion

7.1. Highlight of deformation features captured by P-band InSAR

Another objective of this study was to identify ground deformation features and geohazards near the U.S. West Coast using P-band SAR's unique, combined capabilities of strong vegetation penetration, variable flying path, and relatively high spatial resolution. Here, we highlight six actively deforming features (i.e., landslides) that are found to be near local communities and thus pose potential risk to human safety and infrastructure in the vicinity. Fig. 12a depicts the Oso landslide site in Washington, where a catastrophic slope failure occurred in March 2014 and evolved into a mobile debris flow killing 43 people down the slope within two minutes (Iverson et al., 2015). The P-band InSAR revealed that three parts of the landslide deposits are still deforming. Fig. 12b shows the Montague Creek landslide, which is located approximately 3 km southwest of the Oso landslide. This landslide is covered by dense vegetation and thus difficult to identify from the high-resolution optical image, but its movement was clearly revealed by the P-band SAR interferogram. The similar geological and topographical setting as the Oso landslide indicate that, a runout failure of the Montague Creek landslide could severely damage the community down the slope.

The P-band InSAR also helped to discover two vegetated, small-sized landslides in Washington on which residential houses were built. Fig. 12c illustrates the Aalvik Road landslide in Washington, upon which a dozen of houses are seated. Fresh pavement and cracks near locations where the landslide body crosses Aalvik Road, as observable from the July 2021 high-resolution Google Earth image, also indicate active deformation of this landslide. Fig. 12d pictures the Happy Camp landslide in Washington with a few houses. Fresh cracks and pavement on the Washougal River Road, which crosses the landslide body, confirm its recent activity. The slow movement of both landslides is likely to cause gradual yet continuous damage to the road and houses.

Additionally, with flying headings and left-looking design that are different from the satellite ascending/descending routines, the P-band InSAR allowed to confirm landslide activity and provide supplementary observations from a new look angle. Fig. 12e portrays the Red Bluff landslide (approximately 13 km^2 in size) in Washington. The huge volume of this landslide aroused concerns for its potential future damage to the highway and underground pipelines, and for tsunamigenic runout hazard to the towns on both banks of the Columbia River (Randall, 2012). Previous satellite InSAR observations captured its activity from 2007 to 2019 (Pierson and Lu, 2009; Randall, 2012; Xu et al., 2021b), and the P-band InSAR confirmed its continued slow movement from November 2020 to May 2021 (Fig. 12e). Fig. 12f highlights the Cape Meares landslide on the Oregon coast. A popular coastal town is located downslope of a destabilized section of this landslide complex and could be threatened by future landslide activity. The Cape Meares landslide was documented since 1899, and its recent movement has caused significant destruction to a highway crossing the landslide, leading to a $22 million rerouting project in 2022 to bypass the landslide area (Otak Inc, 2014). The P-band InSAR observations revealed that the landslide continued its slow movement from November 2020 to May 2021, and during this period, no observable runout failures were found from the 3-m-resolution truecolor images (Planet Labs, 2022).

7.2. SAR LOS direction and sensitivity to ground deformation

Unlike the nearly orthogonal observations of optical sensors, the side-looking SAR systems have different sensitivity to ground

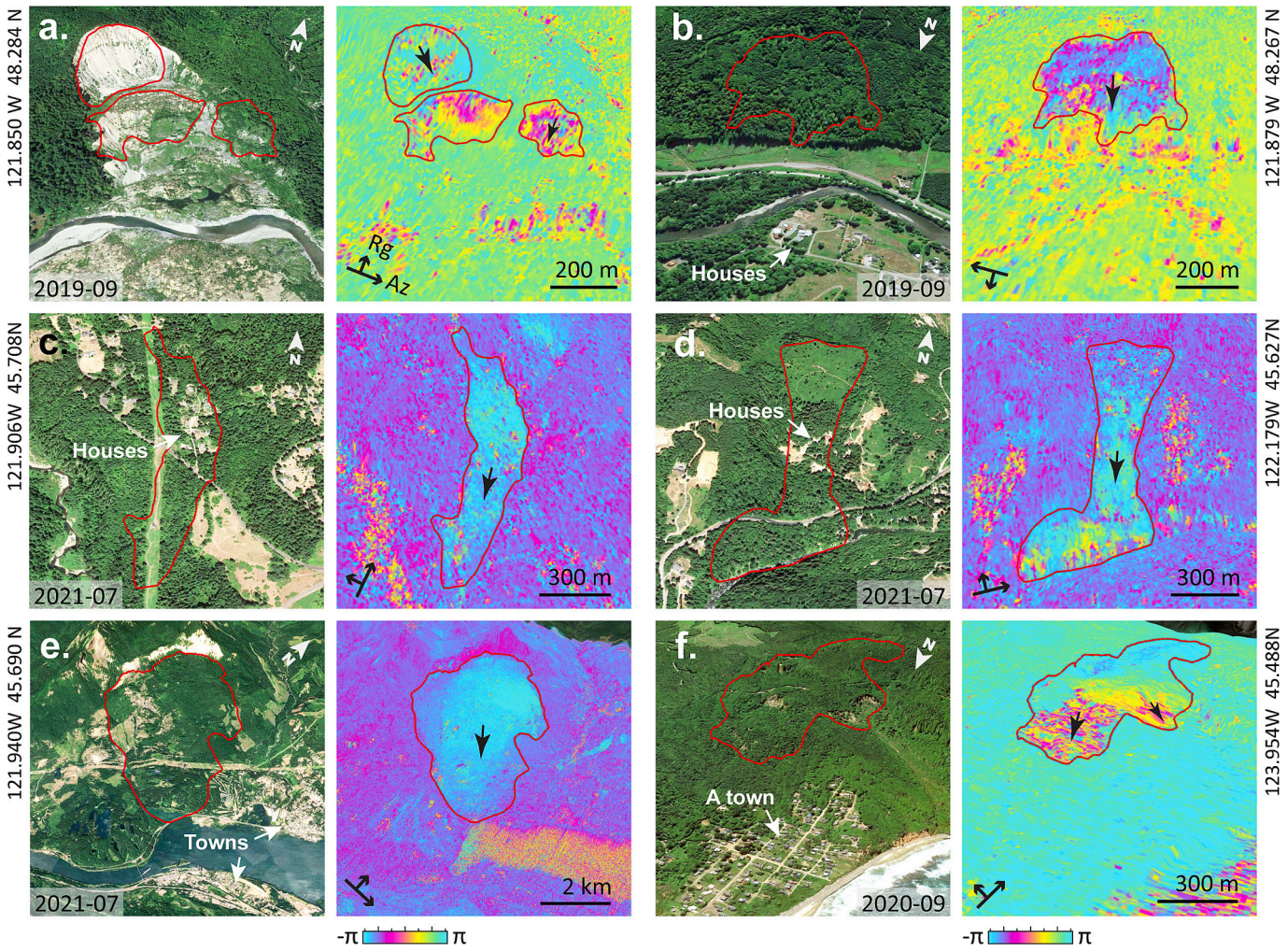

Fig. 12. Active landslides near communities discovered by the P-band InSAR from 13 November 2020 to 30 April 2021. (a) to (f) depict the Google Earth truecolor images and P-band SAR interferograms of the six highlighted landslides. The red polygons and the black arrows inside the polygons denote the boundaries and downslope directions of the landslides, respectively. Geographical coordinates of these landslides are marked on the sides of the images. Acquisition times of the optical images are annotated in the format of "YYYY-MM". A fringe on the SAR interferogram (phase change from $-\pi$ to π) represents a LOS displacement of 34.9 cm. (For interpretation of the references to colour in this figure legend, the reader is referred to the web version of this article.)

displacement depending on both the SAR LOS direction and the ground motion direction. Based on the geometry illustrated in Fig. 2, an arbitrary ground deformation vector $\boldsymbol{D}_{grd}$ can be projected into the radar LOS direction as: $\boldsymbol{D}_{los} = \boldsymbol{D}_{grd} \bullet (\boldsymbol{l} \bullet \boldsymbol{s}^T)$. The value of $(\boldsymbol{l} \bullet \boldsymbol{s}^T)$ decreases as β_{asp} rotates from LOS-parallel to LOS-perpendicular directions (ϕ_{head} to $\phi_{head} \pm 90°$), which indicates decreased sensitivity of the side-looking SAR to ground displacement along commensurate directions in a three-dimensional coordinate system (Xu et al., 2021a). A simplified visualization can be achieved by setting θ_{inc} or ϕ_{head} as the only variable, while other parameters are held constant. Consequently, SAR satellites on the sun-synchronous orbit commonly have lower sensitivity to ground motions along the satellite flying paths (roughly north-south oriented) and higher sensitivity to the west-east oriented movement.

In addition, the Earth's surface topography would inevitably cause blind spots for the side-looking SAR observations owing to the layover (i.e., $\theta_{inc} < \alpha_{slp} < 90°$) and shadow (i.e., $90° - \theta_{inc} < \alpha_{slp} < 90°$) effects (Fig. 2; Rosen et al., 2000). However, the side-looking design could greatly help invert three-dimensional displacement vectors, provided that the same deformation field observed from no less than three independent LOS angles.

For detecting subtle ground deformation, adjusting the SAR LOS direction could make a difference to increase the detection sensitivity (e.g., Xu et al., 2021a). For example, the nearly south-facing Montague Creek landslide (Fig. 12b) was hardly discoverable from the ascending and descending polar-orbit satellite SAR, but was clearly revealed by the west-east flying airborne SAR data. Moreover, the UVASAR P-band system's wide range of incidence angles from 25° to 55° could help reduce the blind spots caused by earth's topography, and the variable looking angles are also beneficial for SAR tomography studies (e.g., Reigber and Moreira, 2000).

7.3. Potential, limitation, and outlook of P-band InSAR

The SAR wavelength λ depends upon the operational frequency f of the radar system as: $\lambda = c/f$, where c is the speed of light. Low-frequency electromagnetic waves (e.g., 430 MHz for the UAVSAR P-band) experience less attenuation and can penetrate to greater depth than the high-frequency X/C/L-band SAR sensors (1–12 GHz). Consequently, P-band SAR systems have unique capabilities for revealing deformation and other signals covered by surficial materials (e.g., vegetation and snow), such as landslides in dense forests (e.g., Xu et al., 2021a), subsurface valleys in desert sands (e.g., McCauley et al., 1982), subglacial groundwater table (e.g., Bessette et al., 2021), and root-zone soil moisture (e.g., Tabatabaeenejad et al., 2014). The greater penetration depth is critical for monitoring densely forested tropical/subtropical zones and snow-covered areas.

For discovering subtle deformation over predominantly barren terrains, the shorter-wavelength X/C/L-band SAR may be more suitable. As demonstrated in Section 5.5, provided that the InSAR coherences only differ slightly, the short-wavelength InSAR tend to have higher measurement precision. Conversely, long-wavelength SAR data are preferred for resolving spatially high-gradient displacements (i.e., large deformation occurring within a localized area), which often lead to significant coherence loss and render the short-wavelength X/C/L-band InSAR measurements ineffective (detailed in Section 5.4). Note that resolving high-gradient displacement of continuously deforming features (e.g., volcanic inflation, slow-moving landslides and glaciers, and creeping faults) could also benefit from temporally dense SAR acquisitions and high pixel resolution.

Presently, the majority of satellite SAR systems operate in the X/C/L bands, and only a few airborne systems are able to collect P-band SAR data, such as German aerospace Center (DLR)'s F-SAR system (Horn et al., 2009) and NASA's UAVSAR P-band system (Chapin et al., 2012). However, to acquire P-band SAR data routinely with global coverage, satellite P-band SAR systems are required. To this end, the ESA (European Space Agency)'s planned P-band BIOMASS mission planned for launch in 2024 has moved us a step forward (Quegan et al., 2019). The designed spatial resolution of 60 m × 50 m (range by azimuth) might be challenging for monitoring localized ground deformation (e.g., small-sized landslides), but potential applications can be found for large deformation features such as volcanoes and faults. The BIOMASS mission's 3-day repeat cycle and dual-baseline configuration, however, can greatly help reduce temporal decorrelation. Additionally, spaceborne SARs operating in P-band are subject to stronger radio frequency interference (RFI) and ionospheric impacts (e.g., Faraday rotation and phase scintillation) in comparison to radars operating in higher frequencies. Nevertheless, studies show that the RFI can be effectively mitigated using variable approaches (e.g., Tao et al., 2019), and the ionospheric influence can be minimized through a dawn-dust orbit design (Rogers et al., 2013). In particular, the Faraday rotation is readily compensated using polarimetric acquisitions (e.g., Freeman, 2004), and the ionospheric phase scintillation can be compensated using fully polarized SAR data and phase gradient autofocus (e.g., Rogers et al., 2013; Li et al., 2015).

8. Conclusions

In recent decades, the relatively short-wavelength X/C/L-band InSAR systems have proven to be powerful tools for measuring earth's surface deformation. However, significant coherence loss resulting from dense forest canopies and fast ground movement remain a challenge for these SAR systems. In this study, we investigate if the longer-wavelength P-band SAR could help address these challenges. By utilizing the NASA JPL's UAVSAR system to collect repeat-pass P-band data over diverse terrains in the U.S. West Coast and both P/L-band SAR data that overlap in the Eel River region (northern California), we conducted a comprehensive evaluation of P-band SAR's performance for detecting and measuring ground deformation. Our results show that, in general, P-band (wavelength≈70 cm) SAR could achieve better InSAR coherence over particularly densely forested areas and lead to more clear signals for deformation surveying than L-band (wavelength≈24 cm) InSAR. Moreover, the P-band InSAR outperformed the shorter-wavelength L-band data for resolving spatially high-gradient ground displacements, which are commonly encountered for slow-moving landslides and ground subsidence caused by underground excavations and fault-bounded aquifers. Partly owing to the variable flying paths, the UAVSAR P-band data helped to discover >200 slow-moving landslides within the study area that were missing from existing landslide inventories. Some of these newly discovered landslides are near communities and could be potential safety threats.

Despite of the above-mentioned advantages, we found that P-band SAR exhibits decreased sensitivity to subtle ground deformation over sparsely vegetated terrains, where the X/C/L-band SAR acquisitions were able to retain high coherence but had relatively lower noise levels. Over the snow-covered terrains in the Cascade Ranges, the P-band SAR was able to able to penetrate though snowpacks thinner than about 1.5 m in vertical depth, and the coherence loss started to increase for much thicker snowpacks.

In summary, the P-band SAR could be a critical supplement for the existing X/C/L-band SAR systems to help survey ground deformation, particularly for the regions where dense forest canopies or spatially high-gradient displacement challenge the performance of the short-wavelength SAR significantly.

CRediT authorship contribution statement

Yuankun Xu: Conceptualization, Methodology, Formal analysis, Investigation, Writing – original draft, Visualization. **Zhong Lu:** Conceptualization, Funding acquisition, Writing – review & editing, Supervision. **Roland Bürgmann:** Writing – review & editing, Supervision. **Scott Hensley:** Resources, Writing – review & editing. **Eric Fielding:** Writing – review & editing. **Jinwoo Kim:** Resources.

Declaration of Competing Interest

The authors declare no conflict of interest.

Data availability

Data will be made available on request.

Acknowledgements

We thank the UAVSAR team of Jet Propulsion Laboratory for helping collect and process the UAVSAR P/L-band data. This study was funded by NASA ESI (Earth Surface & Interior) Program (80NSSC19K1317, 80NSSC22K0461) and NASA Interdisciplinary Research (IDS) in Earth Science Program (80NSSC17K0022). A portion of this work was conducted by the Jet Propulsion Laboratory, California Institute of Technology, under contract with the National Aeronautics and Space Administration. The gridded snowfall data used in this study were accessed from the National Weather Service (https://www.nohrsc.noaa.gov/snowfall/). The SNOTEL snow depth data were accessed from the National Water and Climate Center (https://www.nrcs.usda.gov/wps/portal/wcc/). The UAVSAR P/L-band data used in this study are downloadable at https://uavsar.jpl.nasa.gov/cgi-bin/data.pl.

References

Amelung, F., Galloway, D.L., Bell, J.W., Zebker, H.A., Laczniak, R.J., 1999. Sensing the ups and downs of Las Vegas: InSAR reveals structural control of land subsidence and aquifer-system deformation. Geology 27 (6), 483–486.

Bessette, J.T., Schroeder, D.M., Jordan, T.M., MacGregor, J.A., 2021. Radar-sounding characterization of the subglacial groundwater table beneath Hiawatha glacier, Greenland. Geophys. Res. Lett. 48 (10) e2020GL091432.

Bradford, J.H., Harper, J.T., Brown, J., 2009. Complex dielectric permittivity measurements from ground-penetrating radar data to estimate snow liquid water content in the pendular regime. Water Resour. Res. 45 (8).

Cascini, L., Fornaro, G., Peduto, D., 2010. Advanced low-and full-resolution DInSAR map generation for slow-moving landslide analysis at different scales. Eng. Geol. 112 (1–4), 29–42.

Chapin, E., Chau, A., Chen, J., Heavey, B., Hensley, S., Lou, Y., Moghaddam, M., 2012, May. AirMOSS: An airborne P-band SAR to measure root-zone soil moisture. In: 2012 IEEE Radar Conference. IEEE, pp. 0693–0698.

Didan, K., 2021. MODIS/Terra Vegetation Indices 16-Day L3 Global 500m SIN Grid V061 [Data set]. NASA EOSDIS Land Processes DAAC. Accessed 2022-10-20 from. https://doi.org/10.5067/MODIS/MOD13A1.061.

Dobson, M.C., Ulaby, F.T., Hallikainen, M.T., El-Rayes, M.A., 1985. Microwave dielectric behavior of wet soil-Part II: Dielectric mixing models. IEEE Trans. Geosci. Remote Sens. 1, 35–46.

El Hajj, M., Baghdadi, N., Bazzi, H., Zribi, M., 2018. Penetration analysis of SAR signals in the C and L bands for wheat, maize, and grasslands. Remote Sens. 11 (1), 31.

Freeman, A., 2004. Calibration of linearly polarized polarimetric SAR data subject to Faraday rotation. IEEE Trans. Geosci. Remote Sens. 42 (8), 1617–1624.

Goldstein, R.M., Zebker, H.A., Werner, C.L., 1988. Satellite radar interferometry: two-dimensional phase unwrapping. Radio Sci. 23 (4), 713–720.
Gray, L., 2011. Using multiple RADARSAT InSAR pairs to estimate a full three-dimensional solution for glacial ice movement. Geophys. Res. Lett. 38 (5).
Hallikainen, M.T., Ulaby, F.T., Dobson, M.C., El-Rayes, M.A., Wu, L.K., 1985. Microwave dielectric behavior of wet soil-part 1: Empirical models and experimental observations. IEEE Trans. Geosci. Remote Sens. 1, 25–34.
Handwerger, A.L., Roering, J.J., Schmidt, D.A., Rempel, A.W., 2015. Kinematics of earthflows in the Northern California Coast Ranges using satellite interferometry. Geomorphology 246, 321–333.
Hensley, S., Michel, T., Simard, M., Jones, C., Muellerschoen, R., Le, C., Chapman, B., 2009, May. Residual motion estimation for UAVSAR: implications of an electronically scanned array. In: In 2009 IEEE Radar Conference. IEEE, pp. 1–5.
Hensley, S., Zebker, H., Jones, C., Michel, T., Muellerschoen, R., Chapman, B., 2010, January. Use of airborne SAR interferometry for monitoring deformation of large-scale man-made features. In: International Workshop Spatial Information Technologies, Hong Kong, China.
Hoen, E.W., Zebker, H.A., 2000. Penetration depths inferred from interferometric volume decorrelation observed over the Greenland ice sheet. IEEE Trans. Geosci. Remote Sens. 38 (6), 2571–2583.
Horn, R., Nottensteiner, A., Reigber, A., Fischer, J., Scheiber, R., 2009, July. F-SAR—DLR's new multifrequency polarimetric airborne SAR. In: In 2009 IEEE International Geoscience and Remote Sensing Symposium, vol. 2. IEEE pp. II-902.
Iverson, R.M., George, D.L., Allstadt, K., Reid, M.E., Collins, B.D., Vallance, J.W., Bower, J.B., 2015. Landslide mobility and hazards: implications of the 2014 Oso disaster. Earth Planet. Sci. Lett. 412, 197–208.
Jiang, M., Li, Z.W., Ding, X.L., Zhu, J.J., Feng, G.C., 2011. Modeling minimum and maximum detectable deformation gradients of interferometric SAR measurements. Int. J. Appl. Earth Obs. Geoinf. 13 (5), 766–777.
Jones, E.S., et al., 2019. Summary metadata – landslide inventories across the United States: U.S. Geological Survey data release. https://doi.org/10.5066/P9E2A37P.
JPL (Jet Propulsion Laboratory), 2022. Uninhabited Aerial Vehicle Synthetic Aperture Radar data portal. https://uavsar.jpl.nasa.gov/cgi-bin/data.pl.
Just, D., Bamler, R., 1994. Phase statistics of interferograms with applications to synthetic aperture radar. Appl. Opt. 33 (20), 4361–4368.
Lacroix, P., Handwerger, A.L., Bièvre, G., 2020. Life and death of slow-moving landslides. Nat. Rev. Earth Environ. 1 (8), 404–419.
Li, Z., Elliott, J.R., Feng, W., Jackson, J.A., Parsons, B.E., Walters, R.J., 2011. The 2010 MW 6.8 Yushu (Qinghai, China) earthquake: constraints provided by InSAR and body wave seismology. J. Geophys. Res. Solid Earth 116 (B10).
Li, Z., Quegan, S., Chen, J., Rogers, N.C., 2015. Performance analysis of phase gradient autofocus for compensating ionospheric phase scintillation in BIOMASS P-band SAR data. IEEE Geosci. Remote Sens. Lett. 12 (6), 1367–1371.
Lu, Z., Dzurisin, D., 2014. InSAR imaging of Aleutian volcanoes. In: InSAR imaging of Aleutian volcanoes. Springer, Berlin, Heidelberg, pp. 87–345.
Lu, Z., Meyer, D.J., 2002. Study of high SAR backscattering caused by an increase of soil moisture over a sparsely vegetated area: implications for characteristics of backscattering. Int. J. Remote Sens. 23 (6), 1063–1074.
Madsen, S.N., Zebker, H.A., Martin, J.A.N.M., 1993. Topographic mapping using radar interferometry: processing techniques. IEEE Trans. Geosci. Remote Sens. 31 (1), 246–256.
McCauley, J.F., Schaber, G.G., Breed, C.S., Grolier, M.J., Haynes, C.V., Issawi, B., Blom, R., 1982. Subsurface valleys and geoarcheology of the eastern Sahara revealed by shuttle radar. Science 218 (4576), 1004–1020.
NWS (National Weather Service), 2022. National Gridded Snowfall Analysis. https://www.nohrsc.noaa.gov/snowfall/.
Otak Inc, 2014. Cape Meares Landslide Evaluation and Alternate Route Study. https://www2.co.tillamook.or.us/gov/pw/Documents/Cape%20Meares/Cape%20Meares%20Final%20Technical%20Memo.pdf.
Peplinski, N.R., Ulaby, F.T., Dobson, M.C., 1995. Dielectric properties of soils in the 0.3-1.3-GHz range. IEEE Trans. Geosci. Remote Sens. 33 (3), 803–807.
Perissin, D., Wang, Z., Lin, H., 2012. Shanghai subway tunnels and highways monitoring through Cosmo-SkyMed persistent Scatterers. ISPRS J. Photogramm. Remote Sens. 73, 58–67.
Pierson, T.C., Lu, Z., 2009, October. InSAR detection of renewed movement of a large ancient landslide in the Columbia River Gorge, Washington. In: Proceedings of the Geological Society of America 2009 Annual Meeting, Portland, OR, USA, pp. 18–21.
Planet Labs, 2022. https://www.planet.com.
PRISM Climate Group, 2022. PRISM climate data. https://prism.oregonstate.edu.
Quegan, S., Le Toan, T., Chave, J., Dall, J., Exbrayat, J.F., Minh, D.H.T., Williams, M., 2019. The European Space Agency BIOMASS mission: measuring forest above-ground biomass from space. Remote Sens. Environ. 227, 44–60.
Randall, J.R., 2012. Characterization of the Red Bluff Landslide, Greater Cascade Landslide Complex, Columbia River Gorge. Portland State University, Washington.
Reigber, A., 2001. Correction of residual motion errors in airborne SAR interferometry. Electron. Lett. 37 (17), 1.
Reigber, A., Moreira, A., 2000. First demonstration of airborne SAR tomography using multibaseline L-band data. IEEE Trans. Geosci. Remote Sens. 38 (5), 2142–2152.
Rodriguez, E., Martin, J.M., 1992, April. Theory and design of interferometric synthetic aperture radars. IEE Proceedings F (Radar and Signal Processing) 139 (2), 147–159. IET Digital Library.
Rogers, N.C., Quegan, S., Kim, J.S., Papathanassiou, K.P., 2013. Impacts of ionospheric scintillation on the BIOMASS P-band satellite SAR. IEEE Trans. Geosci. Remote Sens. 52 (3), 1856–1868.
Rosen, P.A., Hensley, S., Joughin, I.R., Li, F.K., Madsen, S.N., Rodriguez, E., Goldstein, R. M., 2000. Synthetic aperture radar interferometry. Proc. IEEE 88 (3), 333–382.
Rosen, P.A., Hensley, S., Wheeler, K., Sadowy, G., Miller, T., Shaffer, S., Madsen, S., 2006, April. UAVSAR: A new NASA airborne SAR system for science and technology research. In: 2006 IEEE Conference on Radar. IEEE, 8-pp.
Schlögel, R., Doubre, C., Malet, J.P., Masson, F., 2015. Landslide deformation monitoring with ALOS/PALSAR imagery: a D-InSAR geomorphological interpretation method. Geomorphology 231, 314–330.
Seymour, M.S., Cumming, I.G., 1994, August. Maximum likelihood estimation for SAR interferometry. In: Proceedings of IGARSS'94-1994 IEEE International Geoscience and Remote Sensing Symposium, Vol. 4. IEEE, pp. 2272–2275.
Singh, A., Meena, G.K., Kumar, S., Gaurav, K., 2018. Analysis of the effect of incidence angle and moisture content on the penetration depth of L-and S-band SAR signals into the ground surface. ISPRS Annals of Photogrammetry, Remote Sensing & Spatial Information Sciences 4 (5).
Smith, D.G., Jol, H.M., 1995. Ground penetrating radar: antenna frequencies and maximum probable depths of penetration in Quaternary sediments. J. Appl. Geophys. 33 (1–3), 93–100.
Tabatabaeenejad, A., Burgin, M., Duan, X., Moghaddam, M., 2014. P-band radar retrieval of subsurface soil moisture profile as a second-order polynomial: first AirMOSS results. IEEE Trans. Geosci. Remote Sens. 53 (2), 645–658.
Tao, M., Su, J., Huang, Y., Wang, L., 2019. Mitigation of radio frequency interference in synthetic aperture radar data: current status and future trends. Remote Sens. 11 (20), 2438.
Techel, F., Pielmeier, C., 2011. Point observations of liquid water content in wet snow–investigating methodical, spatial and temporal aspects. Cryosphere 5 (2), 405–418.
Tiuri, M., Sihvola, A., Nyfors, E.G., Hallikaiken, M., 1984. The complex dielectric constant of snow at microwave frequencies. IEEE J. Ocean. Eng. 9 (5), 377–382.
Ulaby, F.T., Moore, R.K., Fung, A.K., 1982. Microwave Remote Sensing: Active and Passive, vol. 2. Artech House, Norwood, Mass.
USDA, 2022. SNOTEL (SNOwpack TELemetry) and SCAN (Soil Climate Analysis Network). https://www.nrcs.usda.gov/wps/portal/wcc/home/.
USFS (U.S. Forest Service), 2022. Pacific Northwest Forest Inventory and Analysis Databases. https://www.fs.usda.gov/pnw/tools/pnw-fiadb-forest-inventory-and-analysis-databases.
Wang, Z., Yu, S., Tao, Q., Liu, G., Hao, H., Wang, K., Zhou, C., 2018. A method of monitoring three-dimensional ground displacement in mining areas by integrating multiple InSAR methods. Int. J. Remote Sens. 39 (4), 1199–1219.
Wright, T.J., Parsons, B., England, P.C., Fielding, E.J., 2004. InSAR observations of low slip rates on the major faults of western Tibet. science 305 (5681), 236–239.
Xu, Y., Kim, J., George, D.L., Lu, Z., 2019. Characterizing seasonally rainfall-driven movement of a translational landslide using SAR imagery and SMAP soil moisture. Remote Sens. 11 (20), 2347.
Xu, Y., Lu, Z., Kim, J.W., 2021a. P-band InSAR for geohazard detection over forested terrains: preliminary results. Remote Sens. 13 (22), 4575.
Xu, Y., Schulz, W.H., Lu, Z., Kim, J., Baxstrom, K., 2021b. Geologic controls of slow-moving landslides near the US West Coast. Landslides 18 (10), 3353–3365.
Yang, L., Jin, S., Danielson, P., Homer, C., Gass, L., Bender, S.M., Xian, G., 2018. A new generation of the United States National Land Cover Database: requirements, research priorities, design, and implementation strategies. ISPRS J. Photogramm. Remote Sens. 146, 108–123.
Zribi, M., Dechambre, M., 2003. A new empirical model to retrieve soil moisture and roughness from C-band radar data. Remote Sens. Environ. 84 (1), 42–52.